Acta Biomaterialia 165 (2023) 111–124

Contents lists available at ScienceDirect

Acta Biomaterialia

journal homepage: www.elsevier.com/locate/actbio

Full length article

Engineering bone-forming biohybrid sheets through the integration of melt electrowritten membranes and cartilaginous microspheroids☆

Gabriella Nilsson Hall[a,b], Amit Chandrakar[c], Angela Pastore[a,b], Konstantinos Ioannidis[a,b], Katrina Moisley[d], Matei Cirstea[d], Liesbet Geris[a,e,f], Lorenzo Moroni[c], Frank P. Luyten[a], Paul Wieringa[c], Ioannis Papantoniou[a,b,g,*]

[a] Prometheus, Division of Skeletal Tissue Engineering, KU Leuven, Belgium
[b] Skeletal Biology and Engineering Research Center, Department of Development and Regeneration, KU Leuven, Belgium
[c] Department of Complex Tissue Regeneration, Maastricht University, The Netherlands
[d] The Electrospinning Company Ltd, England
[e] Biomechanics Research Unit, Université de Liège, Belgium
[f] Biomechanics Section, KU Leuven, Belgium
[g] Institute of Chemical Engineering Sciences, Foundation for Research and Technology – FORTH, Patras, Greece

ARTICLE INFO

Article history:
Received 6 May 2022
Revised 6 October 2022
Accepted 18 October 2022
Available online 22 October 2022

Keywords:
Melt electrowriting
Spheroids
Endochondral ossification
Developmental engineering

ABSTRACT

Bone fractures are one of the most common traumatic large-organ injuries and although many fractures can heal on their own, 2–12% of fractures are slow healing or do not heal (non-unions). Autologous grafts are currently used for treatment of non-unions but are associated with limited healthy bone tissue. Tissue engineered cell-based products have promise for an alternative treatment method. It was previously demonstrated that cartilaginous microspheroids of periosteum-derived cells could be assembled into scaffold-free constructs and heal murine critically-sized long bone defects (non-unions). However, the handleability of such scaffold-free implants can be compromised when scaling-up. In this work, cartilaginous spheroids were combined with melt electrowritten (MEW) meshes to create an engineered cell-based implant, able to induce *in vivo* bone formation. MEW polycaprolactone meshes were tailored to contain pores (116 ± 28 µm) of a size that captured microspheroids (180 ± 15 µm). Periosteum-derived microspheroids pre-cultured for 4 days, were seeded on MEW meshes and gene expression analysis demonstrated up-regulation of chondrogenic (*SOX9, COL2*) and prehypertrophic (*VEGF*) gene markers after 14 days, creating a biohybrid sheet. When implanted subcutaneously (4 weeks), the biohybrid sheets mineralized (23 ± 3% MV/TV) and formed bone and bone marrow. Bone formation was also observed when implanted in a murine critically-sized long bone defect, though a high variation between samples was detected. The high versatility of this biofabrication approach lies in the possibility to tailor the scaffolds to shape and dimensions corresponding to the large bone defects and the individual patient using robust bone forming building blocks. These strategies are instrumental in the development of personalized regenerative therapies with predictive clinical outcomes.

Statement of significance

Successful treatments for healing of large long bone defects are still limited and 2–12% of fractures do not heal properly. We combined a novel biofabrication technique: melt electrowriting (MEW), with robust biology: bone forming cartilaginous spheroids to create biohybrid sheets able to form bone upon implantation. MEW enabled the fabrication of scaffolds with micrometer-sized fibers in defined patterns which allowed the capturing of and merging with cartilaginous spheroids which had the potency to mature into bone via the developmental process of endochondral ossification. The present study contributes to the rapidly growing field of "Biofabrication with Spheroid and Organoid Materials" and demonstrates

☆ Part of the Special Issue on Biofabrication with Spheroid and Organoid Materials, guest-edited by Professors Mark Skylar-Scott, Heidi Declercq, and Koichi Nakayama.

* Corresponding author at: Skeletal Biology and Engineering Research Center, O&N1 Herestraat 49 - box 813, 3000 Leuven, Belgium.
E-mail address: ioannis.papantoniou@kuleuven.be (I. Papantoniou).

https://doi.org/10.1016/j.actbio.2022.10.037
1742-7061/© 2022 The Authors. Published by Elsevier Ltd on behalf of Acta Materialia Inc. This is an open access article under the CC BY license (http://creativecommons.org/licenses/by/4.0/)

design considerations that are of great importance for biofabrication of functional tissues through the assembly of cellular spheroids.

© 2022 The Authors. Published by Elsevier Ltd on behalf of Acta Materialia Inc.
This is an open access article under the CC BY license (http://creativecommons.org/licenses/by/4.0/)

1. Introduction

Bone is remarkable regarding both mechanical strength and ability to self-renew and heal after injury without creating scar tissue. Despite these properties, bone diseases and traumatic injuries cause widespread problems leading to large bone defects that are unable to regenerate [1,2]. 2–12% of fractures have delayed healing or result in a fracture that is unable to heal (non-union) with tibia non-union having one of the highest prevalence (10–12%) [3,4]. Current treatments for non-unions include stabilization, autografts, allografts and distraction osteogenesis but these treatments are associated with drawbacks, *e.g.*, limited healthy bone tissue, risk of infection, limited vascularization as well as the requirement for additional surgeries [5–7]. The creation of tissue engineered cell-based products gives promise to circumvent the drawbacks of autograft shortage while at the same time being able to heal large bone defects. However, the bone tissue engineering strategy of direct bone formation (intramembranous ossification) has generated limited success for clinical translation [8–11]. Another paradigm called "developmental engineering" has therefore emerged, where engineering strategies are applied to recapitulate developmental and regenerative processes [12,13]. In the case of bone healing, progenitor cells from the periosteum are major contributors in the fracture healing process through the formation of a cartilaginous fracture callus that is remodeled into bone via endochondral ossification [14]. The progenitor cells go through a differentiation cascade from progenitor cells, chondrocytes to hypertrophic chondrocytes which attract blood vessels and transdifferentiate into bone forming osteoblast [15]. Recapitulation of the endochondral ossification process *in vitro* to create a cartilage intermediate that form bone upon implantation has been proven successful in research but presence of necrotic or undifferentiated cells when creating larger cartilaginous *in vitro* tissues pose a challenge for up-scaling [16].

To circumvent diffusion limitations, modular tissue engineering strategies through the use of small scaffold-free "building blocks" (100–300 μm) have recently emerged as a promising strategy to engineer functional tissue implants [17–19]. Scaffold-free building-blocks are created by aggregation of single cells followed by differentiation which results in a tissue with high cell density and endogenous extracellular matrix (ECM). Hence, the tissue structure can have a high resemblance to their corresponding native tissue if suitable culture conditions are maintained. Different building-block configurations have been explored, such as cell sheets [20], tissue strands [21], spheroids [22,23] and organoids [24] but the assembly into larger tissues is linked with difficulties such as diffusion limitations and construct handleability. The building block maturation before assembly, final tissue thickness, host tissue integration as well as biomaterial interaction are parameters which can affect the success of modular tissue engineered implant [25]. Hence, the use of spheroids as "building blocks" requires dedicated studies providing further insights and defined parameters governing spheroid assembly and biomaterial integration [18,26]. It was previously demonstrated that microspheroids of human periosteum derived cells, differentiated towards the chondrogenic lineage, could be assembled into scaffold-free constructs and heal murine critically-sized long bone defects [27]. However, the handleability of such scaffold-free implants can be compromised when scaling-up and creating large pellets (mm) results in necrotic cores or un-differentiated regions [25]. Combining the biologically potent cell modules with advanced biomaterial approaches may be a solution to overcome these hurdles [28].

The development of biomaterials that are conducive for endochondral bone formation is evolving and their use as engineered support structures has potential to create hybrid constructs in combination with cellular micromodules such as spheroids and organoids [29–33]. However, we believe that it is of importance to maintain proper ratios of high cellular density and endogenous ECM to achieve efficient bone formation as demonstrated with assembled microtissues [27]. Bioprinting shows promise for robust biofabrication of tissues and organs with a higher degree of structural organization [34]. In addition to extrusion bioprinting of spheroids in hydrogels [35], combination with other biofabrication techniques such as extrusion thermoplastic polymer dispensing [36,37] or electrospinning [38] have been presented for controlled deposition of spheroids. However, these techniques generate either >100 μm diameter fibers (extrusion) or poorly controlled patterns of micro- and nanofibers (electrospinning). Unlike extrusion and electrospinning technologies, melt electrowriting (MEW) is a relatively new additive manufacturing technology that allows precise fiber deposition similar to extrusion while maintaining micrometer fiber diameters, typically between 2 and 40 μm [39,40]. In MEW, identical to extrusion, molten polymer is forced through a nozzle but in the presence of a high electric field induced between the nozzle and collector plate. This results in the formation of a Taylor cone similar to electrospinning and is thus responsible for thinning the jet. But in comparison to electrospinning, where polymer solutions used are typically mixed with volatile solvents, MEW can process materials in a solvent-free manner that is amenable to clinical grade biomaterials. This would be of importance for future translation into a clinical setting.

In vitro studies using MEW scaffolds have demonstrated cell attachment, cell proliferation and differentiation of single cells towards the osteogenic lineage [41,42]. In addition, MEW meshes have been integrated with cell-laden hydrogels to create reinforced cartilaginous structures [43,44]. Furthermore, implantation of MEW scaffolds with a homogeneous mesh pattern in rat mandibular periodontal fenestration defect model resulted in increased bone formation as compared to empty defects, however these MEW scaffolds did not exhibit any capacity to form bone during subcutaneous implantation [42]. The development of MEW scaffolds with designed porosity to accommodate the integration of spheroids was also recently described for *in vitro* adipogenic differentiation [26]. In this study, we explore the integration of cartilaginous spheroids with MEW scaffolds and their subsequent chondrogenic maturation towards the formation of a biohybrid sheet. Subsequently the *in vivo* functionality of these cartilaginous biohybrid sheets was investigated where bone formation via endochondral ossification was demonstrated.

2. Materials and methods

2.1. Melt-electrowriting of tailored scaffolds

PURASORB® PC 12 with an inherent viscosity midpoint of 1.2 dl/g was obtained from Corbion and used without further modification. MEW was performed using a commercially available MEW system (Spraybase, A-1204-0001-01D), and grid design were con-

ceptualized using python language. Briefly, 1 g of PC_12 pellets was added to the MEW syringe and heated to 80 °C for at least one hour to allow homogenous melting of the polymer. The polymer was then allowed to flow for at least 5 min at high pressure to stabilize the jet flow and ensure a continuous material flow. The collector distance of 5 mm, voltage of 5 kV and pressure of 0.4 bar was kept constant throughout the printing time while moving the collector plate at a critical velocity of 166 mm/s. MEW sheets were printed with ten layers followed by laser cutting using Trotec Speedy 300 Co2 laser engraving machine at 4.3 W, 0.05 m/s speed and 200 Hz frequency, into a defined size (4.5 × 4.5 mm).

2.2. Scaffold characterization

Measurements for fiber diameter, pore size and density were done on three scaffolds with a minimum of three images per scaffold. Imaging and fiber analysis were carried out on a calibrated Phenom XL SEM (Phenom-World) equipped with Fibermetrics analysis software to determine fiber diameter and fiber diameter distribution. The fiber morphologies were imaged on the top surfaces of the membranes. Diameters statistics were established by measuring 100 fibers per image, with three images taken per sample at randomly chosen locations on the membranes. Scaffold pore size was determined using manual measurements of images captured using a calibrated Phenom XL SEM (Phenom-World) and were analyzed using the ImageJ (NIST) software. Due to the rectangular nature of the grid, the value for the pore size is given as the average length of a square.

2.3. Cell isolation and culture

Periosteal biopsies from four donors were digested for cell isolation and a cell pool of human periosteum derived cells (hPDCs) was generated (13 ± 3 years old) as described previously [45]. Patients' informed consent forms were obtained (ML7861) and all procedures were approved by the ethical committee for Human Medical Research (Katholieke Universiteit Leuven). Briefly, the periosteal biopsies were washed and digested in type IV collagenase (440 units/mL, Invitrogen, BE) in growth medium (high-glucose Dulbecco's modified Eagle's medium (DMEM, Invitrogen, BE) supplemented with 10% fetal bovine serum (FBS, Hyclone), and an antibiotic–antimycotic solution (100 μg/ml streptomycin, 100 units/ml penicillin and 0.25 μg/ml amphotericin B, Invitrogen, BE). Next, the digested cells having similar growth kinetics and bone formation capacity were pooled together to create a cell pool. The cell pool was passaged at 90% confluency and expanded until passage 7 (*in vivo*) or 9 (*in vitro* assays) in growth medium at 37°C, 5% CO2 and 95% humidity. Growth medium was changed three times per week until 90% confluency when the cells were harvested using TrypLE™ Express (Life Technologies, UK).

2.4. Microspheroid formation

After harvest, the hPDCs were resuspended in a chemically defined chondrogenic medium (CM) composed of LG-DMEM (Gibco) supplemented with 1% antibiotic-antimycotic (100 units/mL penicillin, 0.25 mg/mL amphotericin B and 100 mg/mL streptomycin), 40 µg/mL proline, 1 mm ascorbate-2 phosphate, 100 nM dexamethasone, ITS+ Premix Universal Culture Supplement (Corning) (including 6.25 µg/mL insulin, 6.25 µg/mL transferrin, 6.25 µg/mL selenious acid, 1.25 µg/mL bovine serum albumin (BSA), and 5.35 µg/mL linoleic acid), 20 µm of Rho-kinase inhibitor Y27632 (Axon Medchem), 100 ng/mL GDF5 (PeproTech), 100 ng/mL BMP-2 (INDUCTOS®), 10 ng/mL TGFβ1 (PeproTech), 1 ng/mL BMP-6 (PeproTech) and 0.2 ng/mL FGF-2 (R&D systems) [46]. Next, 300 000 hPDCs we seeded into an AggreWell™400 (STEMCELL Technologies, DE) microwell platform containing 1200 microwells in each well of a 24 well plate resulting in approximately 250 cells per microspheroid. Microspheroids (here after named spheroids) were cultured with 150 000 cells/mL CM at 37°C, 5% CO2 and 95% humidity and for extended culture time, half of the media was refreshed two times per week.

2.5. Spheroid seeding onto MEW scaffolds and pellet formation

In-house developed non-adherent agarose macrowells (square 5 × 5 mm) were produced using 3D printed negative molds. The negative molds were designed in SolidEdge (Siemens) and printed using Objet30 Prime (Stratasys, US) and VERO white PLUS RGD 835 acrylic resin followed by gas sterilization. Next, 3 mL 3% w/v UltraPure™ agarose (Thermo Fisher) was added to a 12 well plate followed by addition of the negative mold. After the agarose settled, the negative molds were removed, LG-DMEM added and the agarose macrowells were sterilized under UV for 20 min. MEW scaffolds were prewetted in 0.1% Gelatin Solution (Millipore) overnight and then placed within the agarose macrowell. Spheroids of four days were flushed out by pipetting, concentrated by centrifugation, resuspended in 100 µL CM followed by seeding onto the mesh (180 spheroids/mm^2, 3600 spheroids/mesh) in the agarose microwell to form biohybrid sheets. As control, 3600 spheroids were seeded directly into an agarose microwell to form a pellet. CM was added after 1-h incubation at 37°C, 5% CO2 and 95% humidity followed by media change of half the volume three times per week.

2.6. Live/dead staining

Cell viability in biohybrid sheets and pellets was qualitatively assessed on day 7 with LIVE/DEAD® Viability/Cytotoxicity Kit (Invitrogen, USA) for mammalian cells by following the manufacturer's protocol. Briefly, spheroids were rinsed with PBS, where after they were incubated in 2 µm Calcein AM and 4 µm Ethidium homodimer-1 for 30 min at 37°C, 5% CO2 and 95% humidity. Stained samples were imaged with wide-field fluorescence microscopy Olympus IX83 inverted microscope equipped with DP73 camera.

2.7. DAPI/phalloidin staining and nuclei quantification

DAPI/Phalloidin for nuclei quantification was performed on biohybrid sheets and pellets on day 7. Samples were fixated in 4% paraformaldehyde (PFA) overnight at 4°C on a Rocker–Shaker. Next, cell nuclei and filamentous actin (F-actin) were stained with 2.5 µg/mL 4′,6-diamidino-2-phenylindole (DAPI) (Invitrogen) and 0.8 U/mL Alexa Fluor 488® phalloidin (Invitrogen) during 1 h at room temperature on a Rocker-Shaker. Stained spheroids were imaged with an inverted laser scanning fluorescence confocal microscope ZEISS LSM 780 and 880 (Cell and Tissue Imaging Cluster, KU Leuven) with 1 µm thick slices using an argon ion 488 nm and MaiTai® laser. Nuclei in each slice was quantified using thresholding and particle analysis in ImageJ [47].

2.8. Gene expression analysis

Gene expression analysis was performed on day 4 spheroids and after 14 additional days for spheroids, biohybrid sheets and pellets. Biohybrid sheets (mesh + spheroids), pellets and spheroids were washed in PBS and lysed in 400 μL RLT buffer (Qiagen) with 4 μL β-mercaptoethanol (VWR) using FastPrep-24™ system (MP Biomedicals) and Lysing Matrix S-tubes (MP Biomedicals). Total RNA was isolated using QIAshredder (Qiagen) followed by

RNeasy Mini Kit (Qiagen). RNA concentration and quality were assessed with NanoDrop 2000 (Thermo Scientific) and PrimeScript™ RT reagent kit (Takara) was used for complementary DNA (cDNA) synthesis. SYBR® Green (Life Technologies) was used for quantitative real-time polymerase chain reaction (qRT-PCR) on Rotor Gene® 6000 (Qiagen) and the relative differences in expression were calculated using the $2^{-\Delta\Delta Ct}$ method normalized to Hypoxanthine Phosphoribosyltransferase 1 (HPRT1) as housekeeping gene [48]. All protocols were performed according to the manufacturer's protocol.

2.9. In vivo *implantation and explant analysis*

The laser cut meshes (4.5 × 4.5 mm) pre-coated in 0.1% Gelatin Solution (Millipore) overnight and biohybrid sheets' autonomy to form bone tissue was evaluated with a subcutaneous mouse model. Four samples per condition were implanted subcutaneously in immune compromised mice (Rj:NMRInu/nu) and explants were retrieved 4 weeks after implantation and fixed in 4% PFA for subsequent nano-computed tomography (nano-CT). Fixated explants were incubated with the contrast agent Hexabrix® (20% in PBS) and scanned with nano-CT (Pheonix Nanotom M®, GE Measurement and Control Solutions) for 3D visualization and quantification of mineralized tissue. Scans were performed at 60 kV, 140 µA and with diamond target, mode 0, 1 frame average, 0 image skip, 500 ms exposure time, 2400 images and a 0.2 mm aluminum filter resulting in a voxel size of 2 µm. CTAn (Bruker micro-CT, BE) was used for image processing and quantification of mineralized tissue based on automatic Otsu segmentation, 3D space closing and despeckle algorithm. The percentage of mineralized tissue volume (MV) was calculated with respect to the total explant volume (MV/TV). Next, global threshold based on density histogram was applied to threshold scaffold remnants and the percentage of scaffold remnant volume (SV) was calculated with respect to the total explant volume (SV/TV). CTvox (Bruker micro-CT, BE) was used to create 3D visualizations of the mineralized tissue and scaffold.

Next, a critically-sized tibia defect mouse model described elsewhere [49], was used to assess the impact of the environment and mechanical loading on the bone forming potential of the biohybrid sheets. Briefly, an in-house made Ilizarov fixator was used to stabilize the tibia using 27 G steel needles. The tibia was exposed and diamond saw was used to remove a 4 mm mid-diaphyseal segment to create a critically-sized defect as previously demonstrated [27,49,50]. The biohybrid sheets were placed into the defect and the skin was sutured to close the wound. Defects were monitored with *in vivo* micro-CT (SkyScan 1278, Bruker microCT, BE) 0, 4 and 8 weeks after surgery (voxel size of 51 µm). Animals were sacrificed after 8 weeks; the tibia was fixed in 4% PFA and analyzed with *ex vivo* nano-CT and processed for histology. All procedures on animal experiments were approved by the local ethical committee for Animal Research (P36/2016 ECD and P059/2020, KU Leuven), and the animals were housed according to the regulations of the organization.

2.10. Histochemical analysis

Explants were decalcified in ethylenediaminetetraacetic acid (EDTA)/PBS (pH 7.5) for 10 days with changes at 4°C followed by paraffin embedding. Fixated *in vitro* samples and decalcified explants were sectioned at 5 µm for subsequent hematoxylin and eosin (H&E) and safranin O staining according to previously described protocols [7]. The stained slides were imaged with Leica M165 FC microscope (Microsystems, BE) with bright-field and polarized light.

2.11. Statistical analysis

Statistical analysis was performed using GraphPad Prism 9 software (GraphPad Software, Inc., La Jolla, CA) and data was represented as mean ± S.D (Standard Deviation). If nothing else was noted, analysis of Variance followed by Tukey multiple comparison post hoc test was used to find significant differences between the means of the different groups with $p < 0.05$: *, $p < 0.01$: ** and $p < 0.001$: ***.

3. Results

3.1. Melt-electrowritten scaffold tailored for spheroids

MEW printing parameters were first optimized to fabricate a square grid mesh with multiple layers. Printing using the optimized parameters resulted in the generation of sheets with ten layers of PCL fibers creating a network. Scanning electron microscopy (SEM) allowed visualization of the fiber network consisting of stacked PCL fibers with an average fiber diameter of 10.9 ± 2.3 µm and an average sheet thickness of 127 ± 3 μm (Fig. 1A). Next, the multilayered MEW sheets were laser cut into a defined size (4.5 × 4.5 mm) to fit murine tibia defects (Fig. 1B) and the laser cutting resulted in merging of the ten layers allowing easy manipulation of the MEW scaffolds (Fig. 1C). The scaffold pore size, based on top-views, ranged from 50 to 200 µm with an average pore size of 116 ± 28 µm (Fig. 1D). Seeding of single cells onto the scaffolds resulted in a less dense tissue structure (Fig. S 1A) and a lower DNA content as compared to seeding day four spheroids (Fig. S 1B). While single cells fell through the scaffolds, seeding spheroids with a diameter ranging above 100 µm allowed that the cells were captured onto the MEW scaffold (Fig. 1E). The experimental setup was therefore designed, as described in Fig. 1F, with scaffold production, spheroid formation, spheroid seeding and finally chondrogenic differentiation of spheroid on the MEW scaffold. This was followed up by subcutaneous and orthotopic (murine long-bone defect) implantation to assess bone forming capacity.

It was previously reported that hPDC derived spheroids cultured in chondrogenic media have decreased spreading potential onto adherent surfaces with increased spheroid culture time [25]. It was therefore expected that more mature spheroids would attach less also onto the MEW scaffolds. Indeed, seeding day 14 spheroids resulted in aggregation on the border of the scaffolds while the remaining scaffold area was uncovered by cells (Fig. S 1C). Next, spheroids of an earlier time-point (day 4) were seeded since spreading capacity was significantly decreased already after 7 days of spheroid culture according to Nilsson Hall et al. [25] Seeding of day 4 spheroids resulted in improved spheroid attachment to the scaffold (Fig. S 1D). To further improve attachment, 0.1% gelatin coating was added to the scaffold before spheroid seeding (Fig. S 1E). DNA quantification 7 and 14 days after seeding demonstrated an increased number of cells on gelatin coated scaffolds as compared to non-coated scaffolds with aggregated spheroids (pellet) as positive control (Fig. S 1F). The following experiments were performed with gelatin coated scaffolds and day 4 spheroids.

3.2. Spheroids integrate with MEW scaffold to generate a biohybrid sheet

The day 4 spheroids were formed in non-adherent microwells by allowing aggregation of hPDCs (Fig. 2A). The average pore size of the meshes (116 ± 28 µm) was smaller than the average spheroid diameter (180 ± 15 µm) ensuring capture of the spheroids upon seeding (Fig. 2B). Negative molds were 3D printed

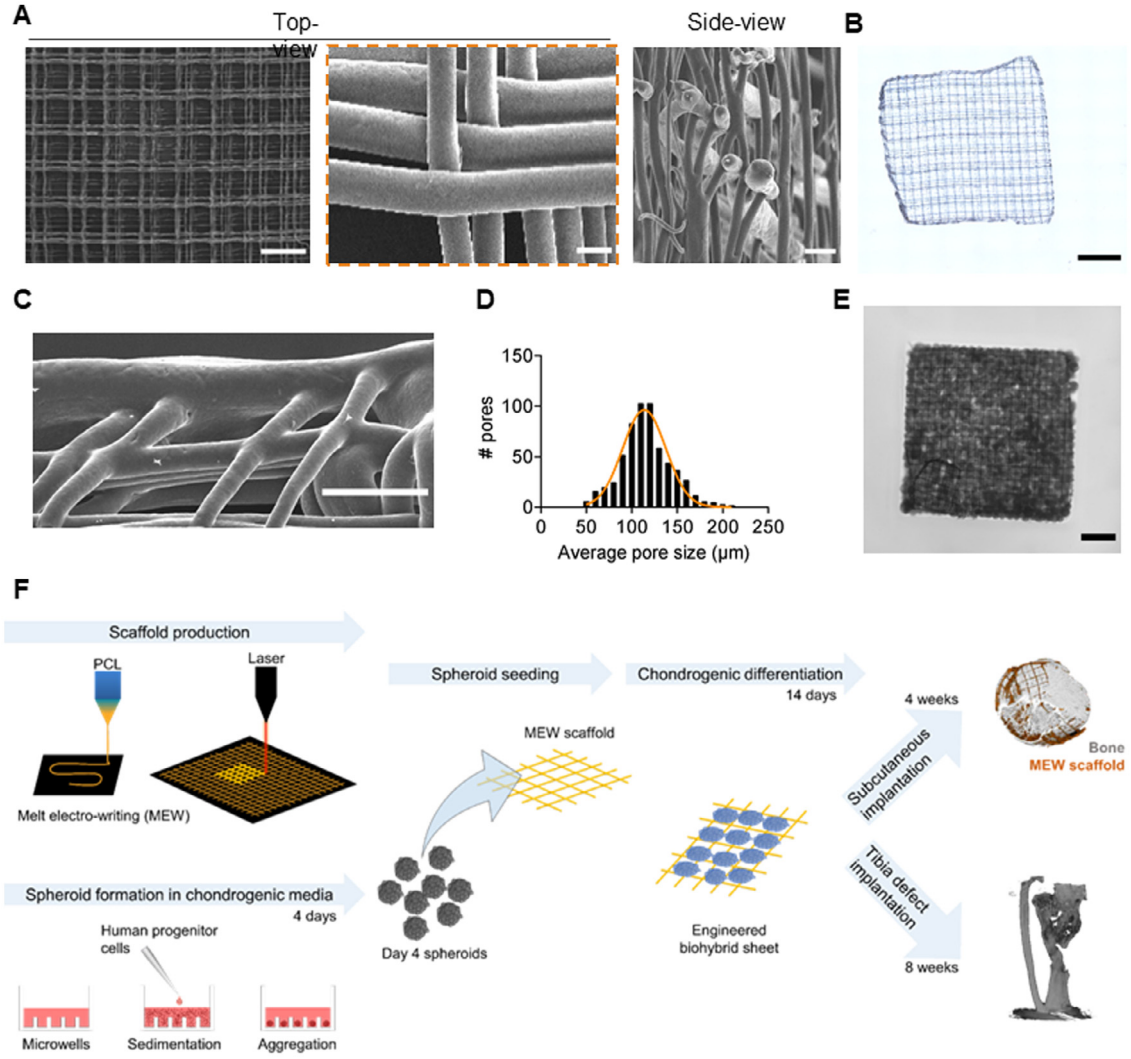

Fig. 1. Fabrication of tailored melt-electro written scaffold for spheroids. (A) Top-view (two magnifications) and side-view SEM images of MEW sheets. (B) Macro-view of printed and laser-cut MEW scaffold. (C) SEM images of a MEW scaffold border after laser cutting. (D) Histogram of the MEW scaffolds pore size. (E) Bright-field image of MEW scaffold with spheroids seeded on top. (F) Schematic overview of the experimental setup. PCL: polycaprolactone, hPDC: human periosteum derived cells. Scale bars represent A top-view: 150 µm, A top-view (zoom-in): 10 µm, A side-view: 20 µm, B: 1 mm, C: 50 µm, E: 1 mm.

(Fig. 2C) to enable the fabrication of non-adherent agarose macrowells with a size adapted for the laser cut MEW scaffolds (Fig. 2D). One hour after seeding, the spheroids had sedimented and covered the MEW scaffold to saturation (Fig. 2E). The spheroids were cultured an additional 14 days on the MEW scaffold to allow differentiation towards hypertrophic chondrocytes and the formation of constructs (Fig. 2F). During this time the area of tissue was quantified over time and between conditions. A significant increase in tissue area from day 7 to day 14 was detected for the pellets while no difference over time was detected for Mesh + spheroids (Fig. 2G). However, the Mesh + spheroids were significantly larger for all timepoints demonstrating that the MEW scaffold was able to retain the tissue area better than spheroids alone (Pellet).

Samples were stained with DAPI and phalloidin to visualize nuclei and actin filaments respectively after 7 days assembly. Z- and 3D projection of confocal images demonstrated presence of nuclei in both conditions and in Mesh + spheroid samples the cells were surrounding the PCL fibers creating a square pattern (Fig. 3A-B). No significant difference in cell density was detected for pellet compared to Mesh + spheroids (Fig. 3C). Quantification of the nuclei in the Mesh + spheroid constructs for each confocal section showed a maximum cell density of 1161 nuclei/mm^2 on the mesh side (Fig. 3D) and 1883 nuclei/mm^2 on the tissue side on which the spheroids were seeded (Fig. 3E). The difference in depth shown on the x-axis of Fig. 3D and E was attributed to limitations in imaging dense tissues with confocal microscopy. Furthermore, brightfield images (Fig. 3F) and live/dead staining (Fig. 3G) demonstrated viable cells in both pellet and Mesh + spheroid constructs. Hence, cells attached and spread over the MEW scaffold to create a biohybrid tissue sheet.

3.3. Biohybrid sheets mature into cartilage intermediates

To ensure that the biohybrid sheets differentiated towards cartilage-like tissue, histological analysis as well as gene expression analysis was performed. H&E staining demonstrated the presence of extracellular matrix (Fig. 4A). A slight curvature in Mesh + Spheroid samples resulted in a hole during paraffin sectioning but sections in other positions demonstrated a complete surface and presence of the mesh (Fig. S2A). Safranin O staining further showed that glycosaminoglycan-rich (cartilaginous) ECM was present in both conditions although mainly in the periphery for pellets (Fig. 4B). Immunostaining showed presence of collagen type 2 in both conditions (Fig. 4C) and hypertrophic-like cells were

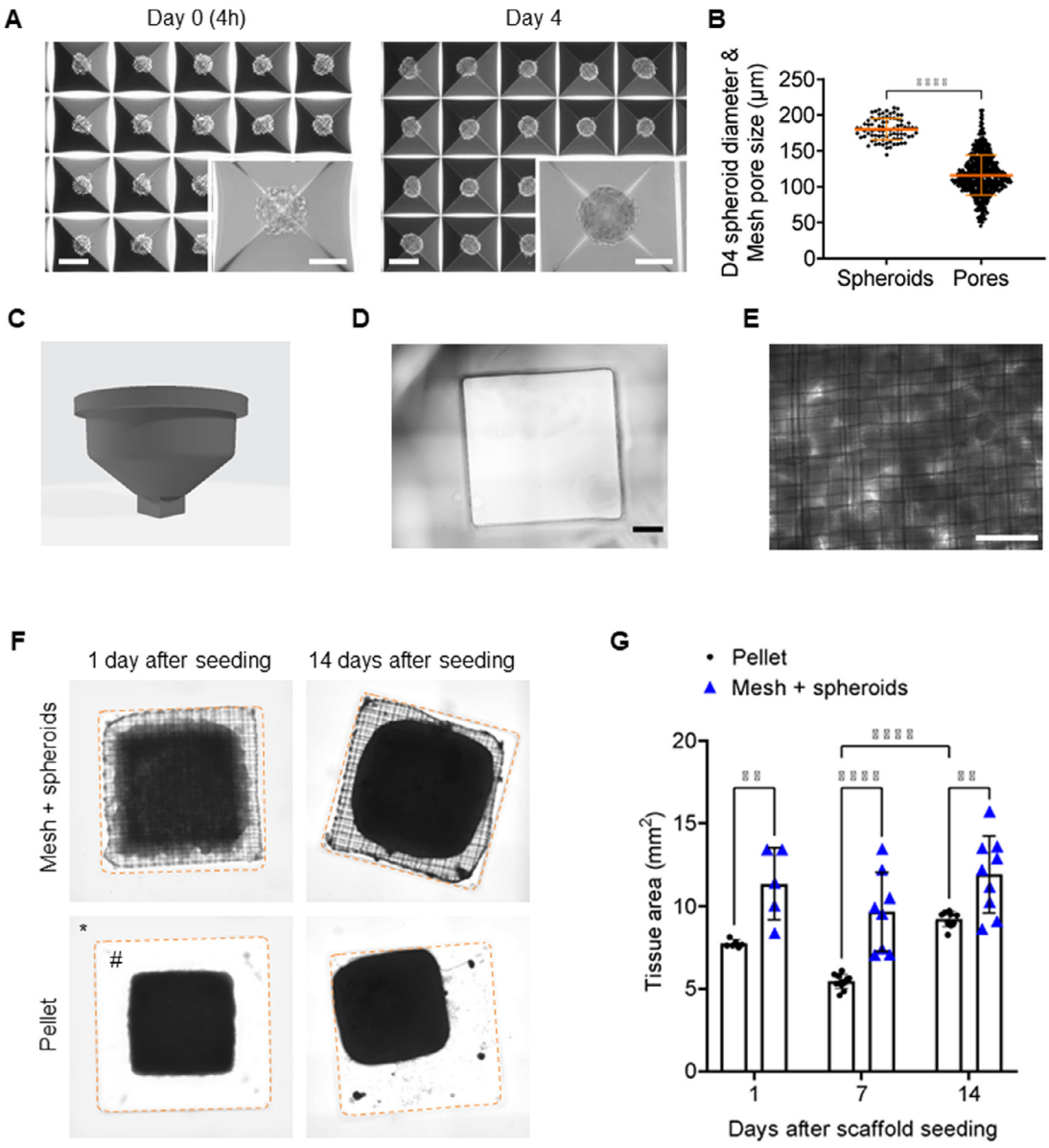

Fig. 2. Creation of MEW scaffold and spheroid biohybrid sheet. (A) Bright-field photos of spheroids 4 h and 4 days after seeding. (B) Graph showing quantified spheroid diameter and MEW scaffold pore size. Each point represents a spheroid or pore size and the average with standard deviation is shown in orange. T-test was performed to statistical comparison with ****: $p < 0.0001$. (C) 3D design of negative mold used to create macro-wells. (D) Bright-field image of macro-mold created in agarose using the 3D negative mold in A. (E) Brightfield image of spheroids seeded onto the MEW scaffold. (F) Bright field images of MEW scaffolds with spheroids and pellets after 1 and 14 days in culture. The orange dashed line represents the macro-well border. (G) The graph shows the quantified tissue area. Each point represents one construct and the average ± std is visualized with black lines for each condition. Two-way ANOVA followed by Tukey's post-hoc test was performed and significant differences are visualized with *: $p < 0.05$, **: $p < 0.01$, ***: $p < 0.001$ and ****: $p < 0.0001$. Scale bars represent A (overview): 200 µm, A (zoom-in insert): 100 µm, D: 1 mm, E: 500 µm.

detected (Fig. S2B, red arrows). The formation of a cartilaginous tissue was further confirmed with gene expression analysis with single spheroids as reference (Fig. 4D). Up-regulation of the chondrogenic markers *SOX9* and *COL2* was present for all conditions after 14 days culture although *SOX9* was higher in Mesh + spheroid and pellet compared to single spheroids. No significant difference was detected in *COL1* gene expression, while *RUNX2* was down-regulated in pellet and Mesh + spheroid. The hypertrophic chondrocyte marker *IHH* was up-regulated in spheroids and pellet with a significantly higher expression in spheroids compared to Mesh + spheroids indicating stronger hypertrophic chondrocyte phenotype in spheroids as compared to Mesh + spheroids. However, *VEGF*, coding for a protein promoting the growth of new blood vessels, was significantly up-regulated in both pellet and Mesh + spheroids but not in single spheroids. These data indicate that the tissue formed in the biohybrid Mesh + spheroid sheets has a cartilage phenotype, although less maturation towards hypertrophy compared to single spheroids.

3.4. *Biohybrid sheets generate bone ossicles* in vivo

To assess if the biohybrid sheets were able to form bone, they were implanted subcutaneously in immunocompromised mice for four weeks and MEW scaffolds alone were implanted as control. Histological analysis of the explants demonstrated that the biohybrid sheets formed bone ossicles containing bone and bone marrow while no bone formation was detected in Meshes only (Fig. 5A). Positive (red) safranin O staining was detected in the biohybrid sheets (Mesh + spheroids) showing that cartilaginous tissue was still present and the large cell size indicated the presence of

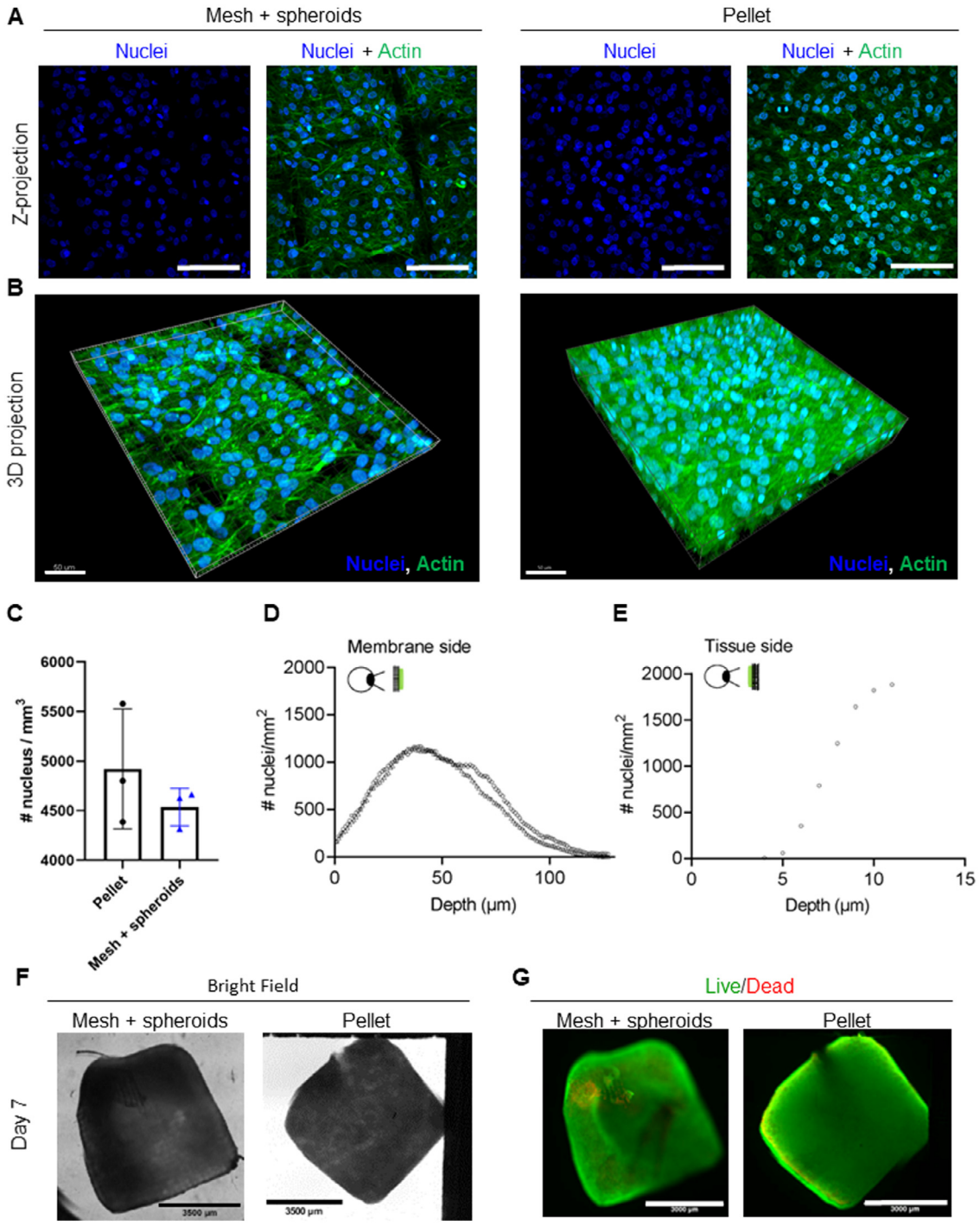

Fig. 3. Cell distribution in biohybrid sheets. (A) Z-projection of confocal images for both conditions. Samples were stained for nuclei (blue) and f-actin (green). (B) 3D projection of the confocal images. (C) Nuclei quantification of z-projections confocal images of pellets and Mesh + spheroid constructs. (D) Nuclei quantification from the scaffold and (E) tissue side of the Mesh + spheroid construct. (F) Bright field and (G) live/dead images of constructs cultured 7 days after spheroids seeding. Scale bars represent A: 100 µm, B: 50 µm and G: 3 mm.

hypertrophic chondrocytes that are known to contribute to continued bone formation (Fig. 5B). No cartilaginous tissue was detected in the mesh samples, while tracks indicative of the MEW scaffold, were visible (orange arrows). Immunostaining of human specific collagen 1 (hCOL1) showed presence of extracellular matrix in the center produced by the implanted cells, while the cortical-like bone was negatively stained indicating that it was produced by mouse cells (Fig. 5C). A similar pattern was detected for human specific osteocalcin (hOCN) staining (Fig. S 2C) and human specific collagen type 2 in tibia explants (Fig. S3B). In conclusion, the human specific immunostaining demonstrated that the implanted cells contributed to the formation of cartilage with hypertrophic cells and bone upon implantation. Finally, nanoCT scan confirmed the presence of mineralized tissue in the biohybrid sheets (23.0 ± 2.9%) with a total explant size of 11 ± 2 mm^3 while no mineralization was detected in the Mesh only samples (Fig. 5D-E). The MEW scaffold within the biohybrid sheets was visible in dark grey (Fig. 5D, orange arrow on section) enabling thresholding

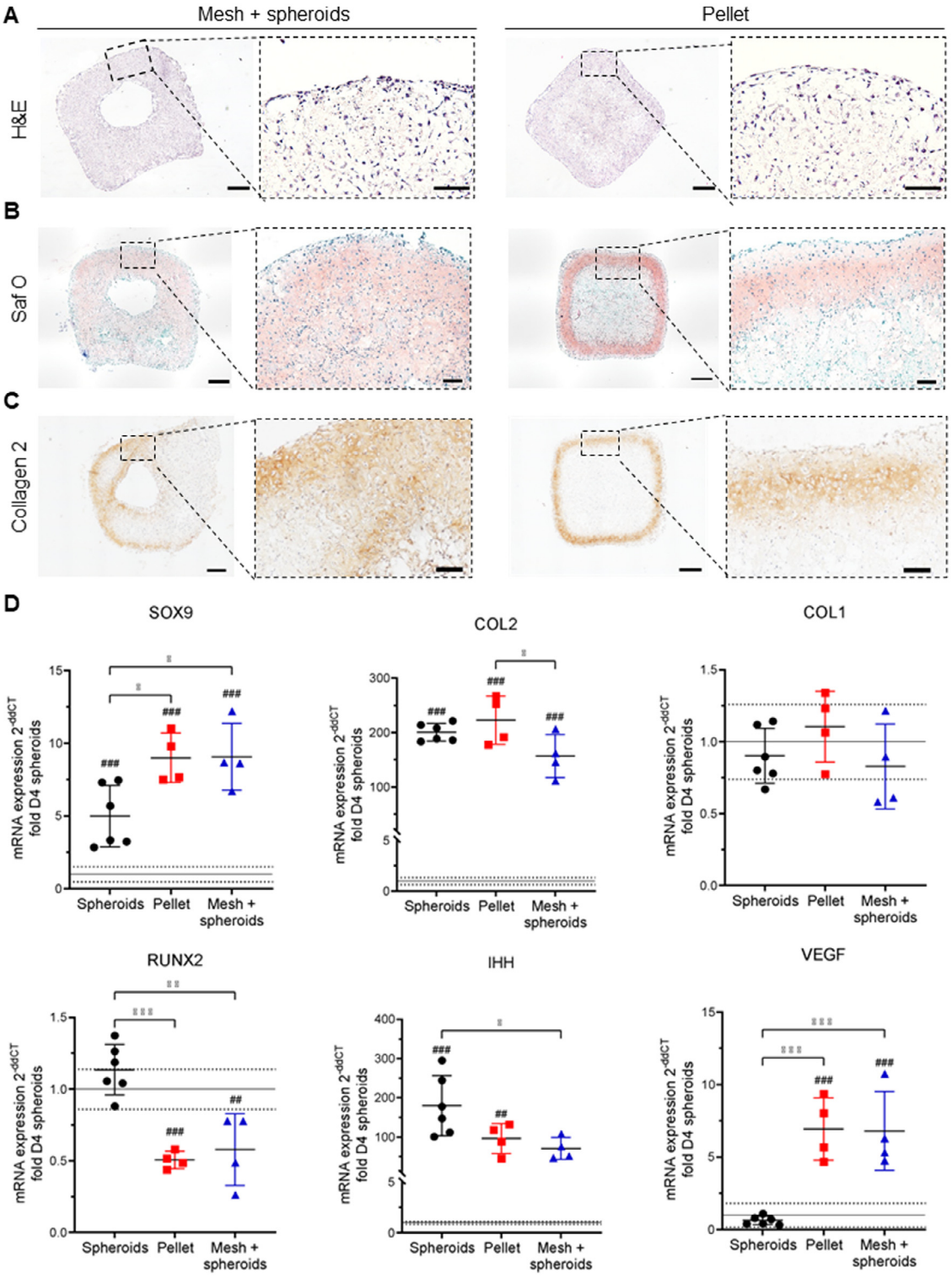

Fig. 4. *In vitro* characterization of biohybrid sheets and pellets. (A) Hematoxylin and Eosin (H&E) and (B) Safranin O and Fast Green (Saf O) staining of Mesh + spheroid constructs and Pellet. Orange arrows point out areas with MEW scaffold. (C) Collagen 2 immunostaining of Mesh + spheroid biohybrid sheets and pellets. (D) Gene expression analysis of gene markers related to chondrogenesis (SOX9, COL2), COL1 and chondrocyte hypertrophy (RUNX2, IHH and VEGF) 14 days after mesh seeding. Day 4 spheroid average (scaffold seeding point) is represented as a black line with stdev as a dashed line. Each point represents one samples and the average ± std per condition is shown. One-way ANOVA followed by Tukey's post-hoc test was performed and significant differences are visualized with *: $p < 0.05$, **: $p < 0.01$ and ***: $p < 0.001$. Scale bars represent A-C (overview): 500 µm and A-C (zoom-in): 100 µm.

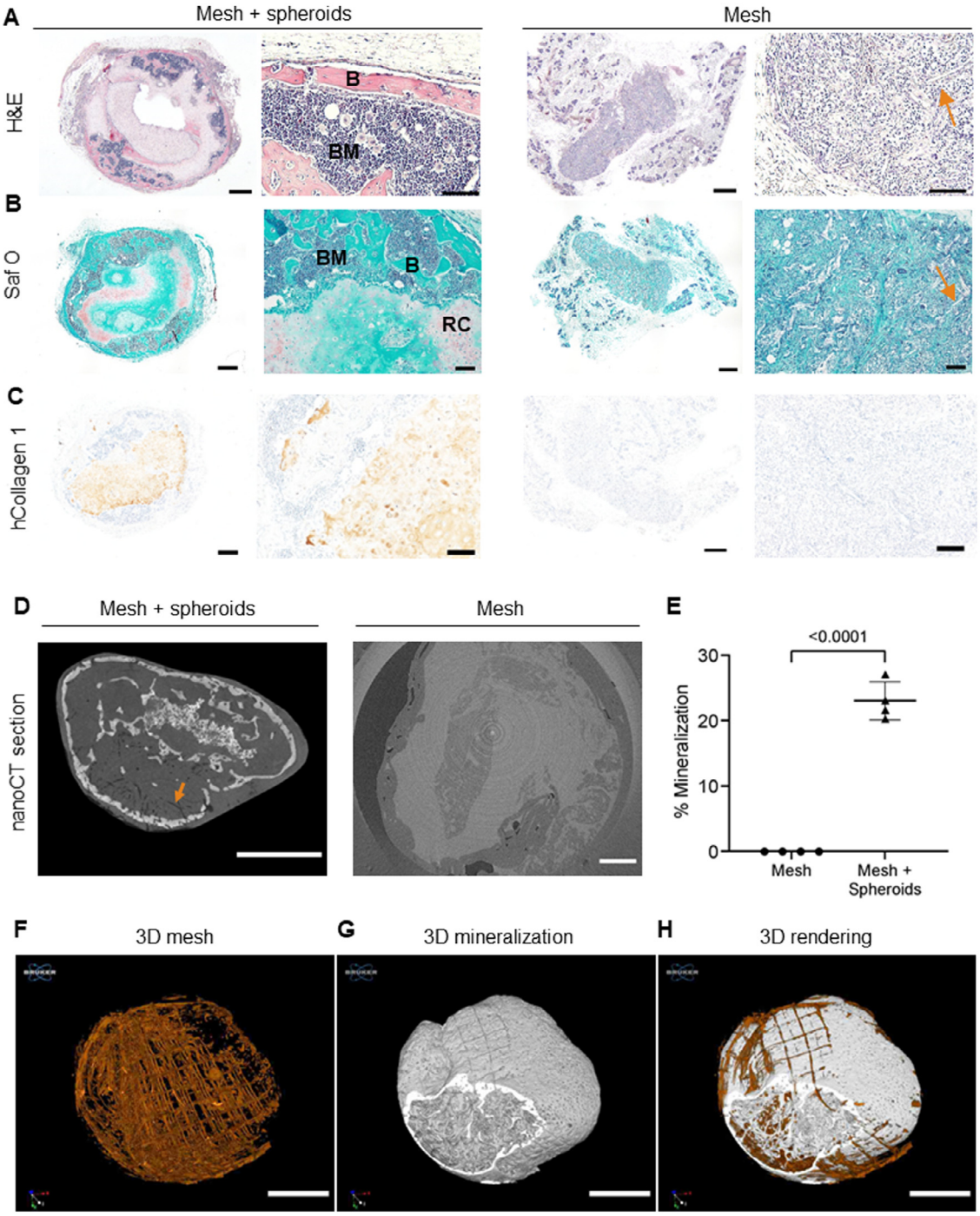

Fig. 5. Bone forming capacity of biohybrid sheets (Mesh + spheroids) and MEW scaffold alone (Mesh) in subcutaneous environment, 4 weeks implantation in immune compromised mice. (A) H&E and (B) Safranin O and Fast Green (Saf O) staining of 4 weeks explants. (C) Human specific collagen type 1 (hCollagen 1) immunostaining of 4 weeks explants. (D) One central image of nanoCT scan with Hexabrix contrast agent. (E) Quantification of mineralized tissue. Each point represents one explant and graph shows average ± std. nanoCT images were used to create 3D renderings of (F) the MEW scaffold (mesh), (G) mineralized tissue and (H) a combination of both the mesh and mineralized tissue. B: bone, BM: bone marrow, RC: remodeling cartilage. Scale bars represent A-C (overview): 500 µm, A-C (zoom-in): 100 µm, D and F-H: 1 mm. (For interpretation of the references to colour in this figure legend, the reader is referred to the web version of this article.)

and 3D rendering of the mesh (Fig. 5F). 3D rendering of the mineralized tissue showed an ossicle containing trabecular bone tissue and the presence of tracks shaped in the pattern of the MEW scaffolds (Fig. 5G). The 3D renderings of the mesh and mineralized tissue were combined to visualize the integration of the MEW scaffold within the newly formed bone (Fig. 5H). The 3D rendered MEW scaffold contributed to only 2.3 ± 0.5% of the total explant volume. In summary, these data demonstrated that the biohybrid sheets were able to form bone organs upon subcutaneous implantation *in vivo* with human cells contributing to the de novo tissue formation.

Next, the biohybrid sheets (Mesh + spheroids) were implanted in a critically-sized murine tibia defect to assess their capacity to heal long bone defects. *In vivo* CT was performed 4 and 8 weeks after implantation to detect mineralization within the defects. Mineralization was detected in all defects with biohybrid sheets although a variation in the amount of mineralization was observed (Fig. 6A). The empty defects contained only a small amount of min-

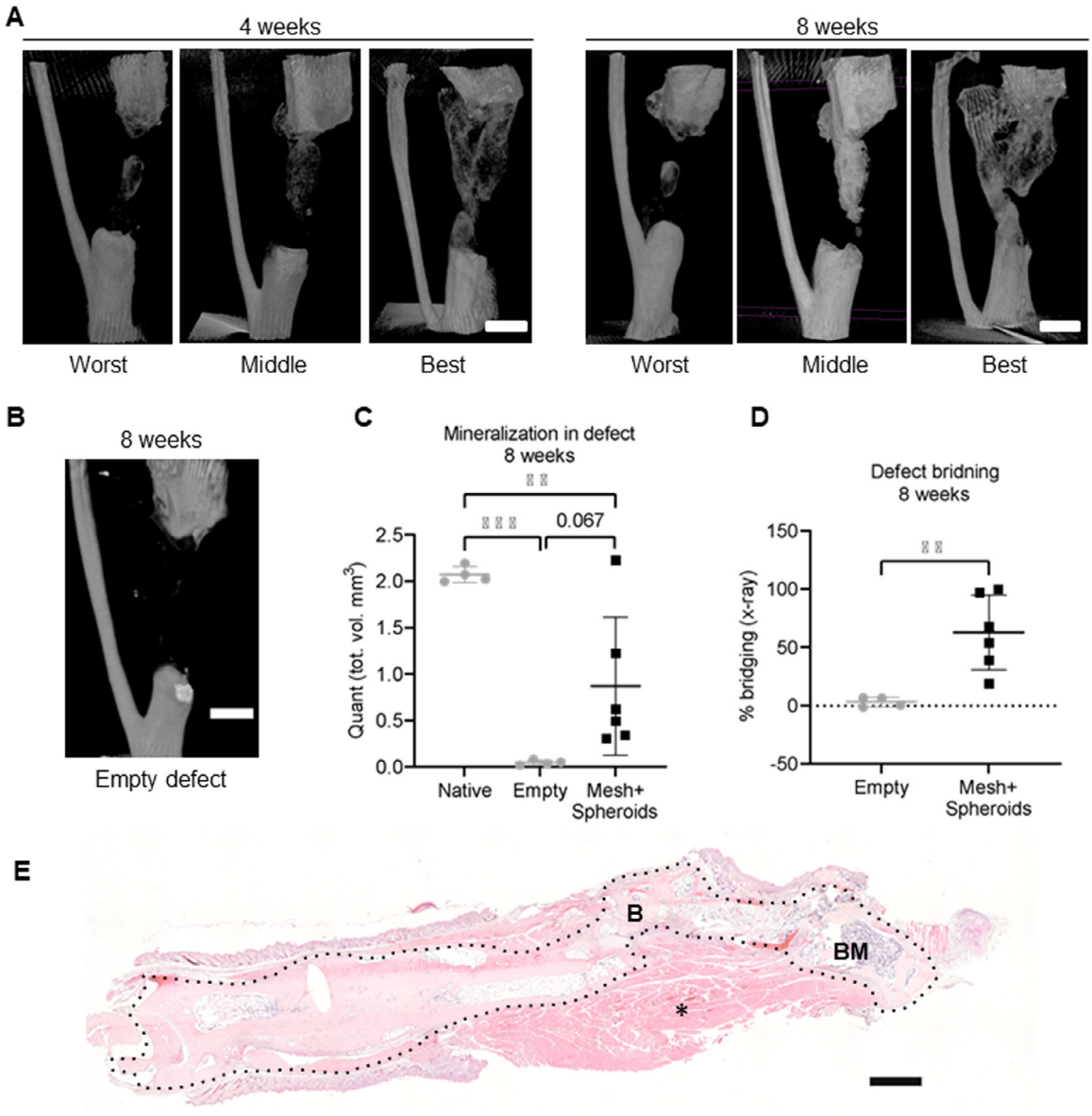

Fig. 6. Implantation of biohybrid sheets in murine critically sized long bone defects. (A) 3D rendering of *in vivo* CT images 4 and 8 weeks after implantation of biohybrid sheets within the defect. Three replicates are shown to demonstrate the worst, middle and best-case scenario. (B) 3D rendering of *in vivo* CT images of an empty defect 8 weeks after surgery. (C) Quantification of total mineralization in defect after 8 weeks implantation. Native tibias (without defect) and empty defects are shown as comparison [27]. (D) Quantification of the percentage of the defect that has been bridged after 8 weeks. Empty defects are shown as comparison [27]. (E) H&E staining of a defect 8 weeks after biohybrid sheet implantation. The dotted line shows the bone area, * the muscle, B bone and BM bone marrow area. C-D: Each point represents one defect in one mouse and graphs show average ± std. Scale bar represents 1 mm.

eralization on the bone edges (Fig. 6B) and both empty defects and experimental defects (Mesh + spheroids) had significantly lower mineralized tissue as compared to native tibia (Fig. 6C). However, the percentage of defect bridging was significantly higher in experimental defects as compared to empty defects (Fig. 6D). The best experimental sample after 8 weeks implantation (Fig. 6A) was stained with H&E demonstrating presence of both bone and bone marrow (Fig. 6E). This data demonstrated that a biohybrid sheet is able to bridge a murine critically-sized tibia defect but a large variation in success rate shows that improvements are required for healing of such defect.

4. Discussion

Successful treatments for healing of large, long bone defects are still limited. The type of fracture, with regard to size and location, as well as the surrounding environment are important parameters for the choice of treatment. Smaller fractures can heal on their own and biomaterial-based bone void fillers (*e.g.* demineralized bone matrix, various ceramics) exist for non-compromised smaller bone defects but healing of large bone defects and non-unions requires a biological alternative [51]. For this, autografts have been traditionally used but limited availability as well as the need for additional surgeries renders this solution suboptimal. Hence, tissue engineering shows promise to meet the demands of highly functional grafts for healing of large bone defects but further improvements are required [52]. The rise of developmental engineering approaches has provided a robust foundation for the engineering of bone forming tissue engineered solutions [16]. In this work, we aimed at generating cartilaginous implants with controlled geometrical features and size using MEW meshes that exhibited high potency to form bone through endochondral ossification upon ectopic implantation.

MEW allows fabrication of well-defined scaffolds from polymer melts but is limited to simple geometry features due to continuous jet motion. In addition, due to residual charges around the deposited fibers, the minimum interfiber distance, i.e., pore size and the number of layers, is currently limited depending on the MEW process and design parameters [53]. With a larger pore size (<1000 µm), it is possible to fabricate a scaffold as high as 7 mm by maintaining a constant electric field with increasing collector distance, although this technique requires a sophisticated MEW system [54]. In this work, we fabricated a scaffold with a smaller pore size (50–200 µm) than the spheroid diameter for effective capturing. MEW scaffolds with larger pore size (360-380 µm) has previously been used for seeding of pre-formed adipose-derived stromal cell spheroids and adipogenic differentiation [55,56]. MEW scaffolds with a pore size of 260 µm were previously used for entrapment of single cell-laden hydrogels which resulted in cell aggregation into spheroids during chondrogenic differentiation [57]. Furthermore, geometric features such as pore size, filament spacing and fiber alignment are shown to affect cellular behavior [41,58,59] and a smaller fiber spacing of 500 µm, as compared to 1100 µm, was shown to influence chondrogenic differentiation of hBMSCs resulting in higher GAG content [60]. With a tailored design, biomaterials can be beneficial also for *in vivo* functionality and scaffolds alone have been demonstrated to promote EO in long bone defects through collagen fiber alignment [61] or improved bone formation with gradient MEW fiber alignment [58]. Hence, the generation of MEW scaffolds with gradient structures could further improve the bone formation of our biohybrid sheets.

Spheroids used in this work were created by aggregating progenitor cells derived from human periosteum. Periosteum as cell source was chosen since cells from the periosteum have been shown to be the main contributors in the formation of the cartilaginous callus during endochondral fracture healing *in vivo* [14,62] and contain skeletal stem cells with high regenerative capacity [63]. The use of cartilage intermediates for bone formation has previously been demonstrated through various strategies [64–67] but linear scale-up to larger chondrogenic *in vitro* constructs, results in non-differentiated regions within the construct [27,68]. The use of micrometer sized spheroids for differentiation into cartilaginous microtissues overcame this problem, however scaffold-free bioassembled constructs exhibit limited handleability [27] which make them difficult to handle. Therefore, combining spheroids with a support material would be instrumental for further upscaling into centimeter sized implants while providing a solution that could be more adapted to surgical handling.

The integration of biomaterials into *in vitro* engineered cartilage intermediates has previously demonstrated successful bone formation upon ectopic implantation by relying on a high initial cell density (20-70 $\times$ 10^6 cells/mL [68–70]) which allows cell-cell contact and appropriate chondrogenic differentiation. The main biomaterials used for *in vivo* endochondral ossification bone formation include hydrogels such as alginate [69,71], gelatin methacrylate (GelMA) [72], fibrin [73] and collagen type I scaffolds alone [68,74–76] or in combination with hyaluronic acid [77] to render mechanical support and at the same time allow cellular maturation. However, diffusion limitations are present also in biomaterial-based constructs [78]. Here, we designed a MEW scaffold that provided a template for seeded spheroids to assemble into biohybrid sheets. The seeding with precondensed spheroids increased dramatically seeding efficiency (and post seeding cell density) as compared to single cells, and appeared to provide a suitable environment for subsequent chondrogenic maturation under the culture conditions as described.

In addition, the biohybrid sheets reduced tissue contraction while still minimizing the extent of foreign scaffold material, generating a larger tissue surface area as compared to scaffold-free constructs with the same number of spheroids (Fig. 2G). This led to larger safranin O positive areas on histological sections (Fig. 4B) which could be a result of reduced tissue thickness [25,78,79]. The reduction in tissue compaction was observed also for biohybrid sheets combining MEW scaffolds and fibrin hydrogel laden with human umbilical cord vein smooth muscle cells [80]. Strategies to maintain tissue size and shape could be further explored by synchronizing the combination of MEW scaffolds with spheroid assembly [22,81,82]. Furthermore, MEW meshes enabled the minimization of foreign polymer material within the explant volume (2.3 $\pm$ 0.5%) compared to three dimensional fused-depositing modeling (FDM) scaffolds. An FDM scaffold with the design of 400 µm filaments and 1 mm (center-to-center) spacing resulted in approximately 31% polymer volume [83]. The use of PCL to generate the MEW scaffold further minimizes this foreign presence by virtue of its slow degradation rate that minimizes local pH shifts, compared to other polymers (*i.e.* poly(glycolic acid) and poly(lactic acid)) which degrade to locally release acidic organic molecules known to trigger immunological responses and inhibit bone formation [84–86].

With previous knowledge in spheroid assembly after chondrogenic differentiation [25] and defined scaffold production, we were able to set up an experimental protocol that allowed spheroid integration with the produced MEW scaffolds. Histology demonstrated larger areas of safranin O positivity in biohybrid sheets as compared to pellet (Fig. 4B) while *COL2* gene expression was down-regulated in biohybrid sheets compared to pellet and single spheroids (Fig. 4D). The difference in *COL2* gene expression could be related with the reduced condensation in biohybrid sheets (Fig. 2F-G), a factor to keep in mind for chondrogenic differentiation [87]. Conversely, the chondrogenic marker *SOX9* was up-regulated in both pellet and biohybrid sheets while the hypertrophic gene markers *RUNX2* and *IHH* were down-regulated, indicating a more pre-hypertrophic phenotype of the spheroids. Interestingly, the angiogenic gene marker *VEGF* was highly up-regulated in both pellet and biohybrid sheets as compared to single spheroids (Fig. 4D) which could be related to lower dissolved oxygen tension [88]. The presence of some areas with fibrous tissue in the explants (Fig. 5A) indicated that the entire *in vitro* tissue did not go through proper chondrogenic differentiation as previously observed for pellet cultures [27,66]. However, *VEGF* is also up-regulated in hypertrophic chondrocytes and important for survival of hypoxic cartilage and the recruitment of vascularization during remodeling of cartilage to bone [89].

Finally, we demonstrated that the “callus”-like living biohybrid sheets developed in this study was able to further mature upon subcutaneous implantation and form bone ossicles with corticalization, bone marrow and remodeling cartilage present (Fig. 5). The remnants of the MEW scaffold were well integrated with the de novo mineralized tissue. Subcutaneous bone ossicle formation has previously been demonstrated in other types of constructs [16], among others using cartilaginous scaffold-free [27] and cells in combination with other types of biomaterials such as type 1 collagen mesh constructs [68]. Bone and bone marrow were also detected in defects with the biohybrid sheet implanted (Fig. 6E) but a variation in success was observed for the orthotopic implantations (Fig. 6A, C-D). Bone and cartilage do not naturally form in a subcutaneous location and chondro- and osteo-inductive signals must therefore arise from the construct itself making it a suitable *in vivo* model to analyze constructs’ autonomy. However, the subcutaneous environment does not fully correlate to the environment of a fracture where vascularization, growth factors and cell availability differs [1], which may be an explanation for the variation in success of the orthotopic experiment.

Given its structure, its improved handleability and osteogenic properties, we envisage these biohybrid implants as foldable sheets

able to wrap around bone defects and promote healing with their enhanced bioactivity. For clinical application, in load bearing defects external fixators are routinely used to prevent excessive loading. However, an improvement of the mechanical stability of the implant, could be achieved in the future through a combination of internal (biodegradable) and flexible external support with load-bearing properties. Moreover wehn scaling up defect dimensions, in case the regenerative capacity of the engineered implants is compromised, alternative approaches could be imagined through the combination with commercial ceramic carriers (i.e. CopiOs, Nu-Oss etc) or even with bone grafts. In this context it is suggested while the bio-hybrid membrane will be wrapped around the defect to actively induce bone formation as previously suggested [90].

5. Disclosures

The authors Katrina Mosley and Matei Cirstea are employed at the Electrospinning Company Ltd, England. The author Gabriella Nilsson Hall is currently employed by Astra Zeneca, Sweden.

Declaration of Competing Interest

The authors declare the following financial interests/personal relationships which may be considered as potential competing interests:

The authors Katrina Mosley and Matei Cirstea are employed at the Electrospinning Company Ltd, England.

Acknowledgment

We acknowledge Kathleen Bosmans for performing *in vivo* experiments; Margot Vergauwen, Inge Van Hoven and Orely Vanborren for cell culture and histological assistance; Carla Geeroms and Janne Vleminckx for technical assistance with the micro-CT; Joris Bleukx for technical assistance with 3D design and printing. Research was funded by BONE Interreg North West Europe (NWE 497), the Research Foundation Flanders (FWO) I.P.: 12O7916N, and CARTiPLEX: G0A4718N, the Horizon 2020 Framework Program (H2020/2014-2021)/ERC (772418), the special research fund of the KU Leuven (GOA/13/016 and C24/17/077), European Regional Development Fund. The project leading to this publication has received funding from the European Union's Horizon 2020 research and innovation programme under grant agreement No 874837. This work was supported by the partners of Regenerative Medicine Crossing Borders (http://www.regmedxb.com). Powered by Health—Holland, and Top Sector Life Sciences & Health. Images were recorded on a Zeiss LSM 880 – Airyscan (Cell and Tissue Imaging Cluster (CIC), Supported by Hercules AKUL/15/37_GOH1816N and FWO G.0929.15 to Pieter Vanden Berghe, University of Leuven. The micro- (or nano-) CT images have been generated on the X-ray computed tomography facility of the Department of Development and Regeneration of the KU Leuven, financed by the Hercules Foundation (project AKUL/13/47).

Supplementary materials

Supplementary material associated with this article can be found, in the online version, at doi:10.1016/j.actbio.2022.10.037.

References

[1] R. Marsell, T.A. Einhorn, The biology of fracture healing, Injury 42 (2011) 551–555, doi:10.1016/j.injury.2011.03.031.
[2] G. Calori, W. Albisetti, A. Agus, S. Iori, L. Tagliabue, Risk factors contributing to fracture non-unions, Injury 38 (2007) S11–S18, doi:10.1016/S0020-1383(07)80004-0.
[3] H.L. Dailey, K.A. Wu, P.S. Wu, M.M. McQueen, Court-brown, tibial fracture nonunion and time to healing after reamed intramedullary nailing: risk factors based on a single-center review of 1003 patients, J. Orthop. Trauma 32 (2018) e263–e269, doi:10.1097/BOT.0000000000001173.
[4] J.D. Thomas, J.L. Kehoe, Bone Nonunion, StatPearls, Treasure Isl, Treasure Island (FL), 2022.
[5] G.M. Calori, E. Mazza, M. Colombo, C. Ripamonti, The use of bone-graft substitutes in large bone defects: any specific needs? Injury 42 (2) (2011) S56–S63 Suppl, doi:10.1016/j.injury.2011.06.011.
[6] M.A. Flierl, W.R. Smith, C. Mauffrey, K. Irgit, A.E. Williams, E. Ross, G. Peacher, D.J. Hak, P.F. Stahel, Outcomes and complication rates of different bone grafting modalities in long bone fracture nonunions: a retrospective cohort study in 182 patients, J. Orthop. Surg. Res. 8 (2013) 1, doi:10.1186/1749-799X-8-33.
[7] J.K. McEwan, H.C. Tribe, N. Jacobs, N. Hancock, A.A. Qureshi, D.G. Dunlop, R.O.C. Oreffo, Regenerative medicine in lower limb reconstruction, Regen. Med. 13 (2018) 477–490, doi:10.2217/rme-2018-0011.
[8] G. Cossu, M. Birchall, T. Brown, P. De Coppi, E. Culme-Seymour, S. Gibbon, J. Hitchcock, C. Mason, J. Montgomery, S. Morris, F. Muntoni, D. Napier, N. Owji, A. Prasad, J. Round, P. Saprai, J. Stilgoe, A. Thrasher, J. Wilson, Lancet commission: stem cells and regenerative medicine, Lancet 6736 (2017) 883–910, doi:10.1016/S0140-6736(17)31366-1.
[9] Bethesda (MD): National Library of Medicine, (US), ClinicalTrials.gov, identifier: "fractures, bone" "cells." (2000). https://clinicaltrials.gov/ct2/results?cond=Fractures%2C+Bone&term=cells&cntry=&state=&city=&dist= (accessed March 3, 2020).
[10] Bethesda (MD): National Library of Medicine, ClinicalTrials.gov, identifier: "cartilage defects" "cells." (2000). https://clinicaltrials.gov/ct2/results?term=cells&cond=Cartilage+defect (accessed March 3, 2020).
[11] G.M. Crane, S.L. Ishaug, A.G. Mikos, Bone tissue engineering, Nat. Med. (1995), doi:10.1038/nm1295-1322.
[12] P. Lenas, M. Moos, F.P. Luyten, Developmental engineering: a new paradigm for the design and manufacturing of cell-based products. Part II. From genes to networks: tissue engineering from the viewpoint of systems biology and network science, Tissue Eng. Part B Rev. 15 (2009) 395–422, doi:10.1089/ten.teb.2009.0461.
[13] P. Lenas, M. Moos, F.P. Luyten, Developmental engineering: a new paradigm for the design and manufacturing of cell-based products. Part I: from three-dimensional cell growth to biomimetics of *in vivo* development, Tissue Eng. Part B Rev. 15 (2009) 381–394, doi:10.1089/ten.TEB.2008.0575.
[14] T.A. Einhorn, L.C. Gerstenfeld, Fracture healing: mechanisms and interventions, Nat. Rev. Rheumatol. 11 (2015) 45–54, doi:10.1038/nrrheum.2014.164.
[15] P. Aghajanian, S. Mohan, The art of building bone: emerging role of chondrocyte-to-osteoblast transdifferentiation in endochondral ossification, Bone Res. 6 (2018) 19, doi:10.1038/s41413-018-0021-z.
[16] I. Papantoniou, G. Nilsson Hall, N. Loverdou, R. Lesage, T. Herpelinck, L. Mendes, L. Geris, Turning nature's own processes into design strategies for living bone implant biomanufacturing: a decade of developmental engineering, Adv. Drug Deliv. Rev. 169 (2021) 22–39, doi:10.1016/j.addr.2020.11.012.
[17] L. Ouyang, J.P.K. Armstrong, M. Salmeron-Sanchez, M.M. Stevens, Assembling Living building blocks to engineer complex tissues, Adv. Funct. Mater. 1909009 (2020) 1–22, doi:10.1002/adfm.201909009.
[18] M.W. Laschke, M.D. Menger, Life is 3D: boosting spheroid function for tissue engineering, Trends Biotechnol. 35 (2017) 133–144, doi:10.1016/j.tibtech.2016.08.004.
[19] R. Burdis, D.J. Kelly, Biofabrication and bioprinting using cellular aggregates and microtissues for the engineering of musculoskeletal tissues, Acta Biomater. (2021), doi:10.2139/ssrn.3739622.
[20] A.M. McDermott, S. Herberg, D.E. Mason, J.M. Collins, H.B. Pearson, J.H. Dawahare, R. Tang, A.N. Patwa, M.W. Grinstaff, D.J. Kelly, E. Alsberg, J.D. Boerckel, Recapitulating bone development through engineered mesenchymal condensations and mechanical cues for tissue regeneration, Sci. Transl. Med. 11 (2019), doi:10.1126/scitranslmed.aav7756.
[21] Y. Yu, K.K. Moncal, J. Li, W. Peng, I. Rivero, J.A. Martin, I.T. Ozbolat, Three-dimensional bioprinting using self-assembling scalable scaffold-free "tissue strands" as a new bioink, Sci. Rep. 6 (2016) 28714, doi:10.1038/srep28714.
[22] T.G. Kim, S.H. Park, H.J. Chung, D.Y. Yang, T.G. Park, Hierarchically assembled mesenchymal stem cell spheroids using biomimicking nanofilaments and microstructured scaffolds for vascularized adipose tissue engineering, Adv. Funct. Mater. 20 (2010) 2303–2309, doi:10.1002/adfm.201000458.
[23] S. Bhumiratana, R.E. Eton, S.R. Oungoulian, L.Q. Wan, G. a Ateshian, G. Vunjak-Novakovic, Large, stratified, and mechanically functional human cartilage grown *in vitro* by mesenchymal condensation, Proc. Natl. Acad. Sci. U. S. A. 111 (2014) 6940–6945, doi:10.1073/pnas.1324050111.
[24] M.A. Skylar-Scott, S.G.M. Uzel, L.L. Nam, J.H. Ahrens, R.L. Truby, S. Damaraju, J.A. Lewis, Biomanufacturing of organ-specific tissues with high cellular density and embedded vascular channels, Sci. Adv. 5 (2019) eaaw2459, doi:10.1126/sciadv.aaw2459.
[25] G.N. Hall, I. Rutten, J. Lammertyn, J. Eberhardt, L. Geris, F.P. Luyten, I. Papantoniou, Cartilaginous spheroid-assembly design considerations for endochondral ossification: towards robotic-driven biomanufacturing, Biofabrication 13 (2021) 045025, doi:10.1088/1758-5090/ac2208.
[26] A. Ovsianikov, A. Khademhosseini, V. Mironov, The synergy of scaffold-based and scaffold-free tissue engineering strategies, Trends Biotechnol. 36 (2018) 348–357, doi:10.1016/j.tibtech.2018.01.005.
[27] G.N. Hall, L.F. Mendes, C. Gklava, L. Geris, F.P. Luyten, I. Papantoniou, Devel-

opmentally engineered callus organoid bioassemblies exhibit predictive *in vivo* long bone healing, Adv. Sci. 7 (2020) 1–16, doi:10.1002/advs.201902295.
[28] Y. Yajima, M. Yamada, R. Utoh, M. Seki, Collagen microparticle-mediated 3D cell organization: a facile route to bottom-up engineering of thick and porous tissues, ACS Biomater. Sci. Eng. 3 (2017) 2144–2154, doi:10.1021/acsbiomaterials.7b00131.
[29] P.S. Lienemann, M.P. Lutolf, M. Ehrbar, Biomimetic hydrogels for controlled biomolecule delivery to augment bone regeneration, Adv. Drug Deliv. Rev. 64 (2012) 1078–1089, doi:10.1016/j.addr.2012.03.010.
[30] N. Gjorevski, A. Ranga, M.P. Lutolf, Bioengineering approaches to guide stem cell-based organogenesis, Development 141 (2014) 1794–1804, doi:10.1242/dev.101048.
[31] E.J. Sheehy, D.J. Kelly, F.J. O'Brien, Biomaterial-based endochondral bone regeneration: a shift from traditional tissue engineering paradigms to developmentally inspired strategies, Mater. Today Biol. 3 (2019) 100009, doi:10.1016/j.mtbio.2019.100009.
[32] P.D. Dalton, T.B.F. Woodfield, V. Mironov, J. Groll, Advances in hybrid fabrication toward hierarchical tissue constructs, Adv. Sci. (2020) 1902953, doi:10.1002/advs.201902953.
[33] C. Vinatier, J. Guicheux, Cartilage tissue engineering: From biomaterials and stem cells to osteoarthritis treatments, Ann. Phys. Rehabil. Med. 59 (2016) 139–144, doi:10.1016/j.rehab.2016.03.002.
[34] C. Mota, S. Camarero-Espinosa, M.B. Baker, P. Wieringa, L. Moroni, Bioprinting: from tissue and organ development to *in vitro* models, Chem. Rev. (2020), doi:10.1021/acs.chemrev.9b00789.
[35] L. De Moor, S. Fernandez, C. Vercruysse, L. Tytgat, M. Asadian, N. De Geyter, S. Van Vlierberghe, P. Dubruel, H. Declercq, Hybrid bioprinting of chondrogenically induced human mesenchymal stem cell spheroids, Front. Bioeng. Biotechnol. 8 (2020) 1–20, doi:10.3389/fbioe.2020.00484.
[36] A.C. Daly, D.J. Kelly, Biofabrication of spatially organised tissues by directing the growth of cellular spheroids within 3D printed polymeric microchambers, Biomaterials 197 (2019) 194–206, doi:10.1016/j.biomaterials.2018.12.028.
[37] I.T. Ozbolat, H. Chen, Y. Yu, Development of "Multi-arm Bioprinter" for hybrid biofabrication of tissue engineering constructs, Robot. Comput. Integr. Manuf. 30 (2014) 295–304, doi:10.1016/j.rcim.2013.10.005.
[38] S. Sankar, C.S. Sharma, S.N. Rath, Enhanced osteodifferentiation of MSC spheroids on patterned electrospun fiber mats - an advanced 3D double strategy for bone tissue regeneration, Mater. Sci. Eng. C 94 (2019) 703–712, doi:10.1016/j.msec.2018.10.025.
[39] T.M. Robinson, D.W. Hutmacher, P.D. Dalton, The next frontier in melt electrospinning: taming the jet, Adv. Funct. Mater. 29 (2019), doi:10.1002/adfm.201904664.
[40] J.C. Kade, P.D. Dalton, Polymers for melt electrowriting, Adv. Healthc. Mater. 2001232 (2021) 1–18, doi:10.1002/adhm.202001232.
[41] C.M. Brennan, K.F. Eichholz, D.A. Hoey, The effect of pore size within fibrous scaffolds fabricated using melt electrowriting on human bone marrow stem cell osteogenesis, Biomed. Mater. 14 (2019), doi:10.1088/1748-605X/ab49f2.
[42] A. Daghrery, J.A. Ferreira, I.J. de Souza Araújo, B.H. Clarkson, G.J. Eckert, S.B. Bhaduri, J. Malda, M.C. Bottino, A highly ordered, nanostructured fluorinated CaP-coated melt electrowritten scaffold for periodontal tissue regeneration, Adv. Healthc. Mater. 10 (2021) 1–19, doi:10.1002/adhm.202101152.
[43] M. de Ruijter, A. Ribeiro, I. Dokter, M. Castilho, J. Malda, Simultaneous micropatterning of fibrous meshes and bioinks for the fabrication of living tissue constructs, Adv. Healthc. Mater. 8 (2019), doi:10.1002/adhm.201800418.
[44] J.H. Galarraga, R.C. Locke, C.E. Witherel, B.D. Stoeckl, M. Castilho, R.L. Mauck, J. Malda, R. Levato, J.A. Burdick, Fabrication of MSC-laden composites of hyaluronic acid hydrogels reinforced with MEW scaffolds for cartilage repair, Biofabrication 14 (2022), doi:10.1088/1758-5090/ac3acb.
[45] J. Eyckmans, S.J. Roberts, J. Schrooten, F.P. Luyten, A clinically relevant model of osteoinduction: a process requiring calcium phosphate and BMP/Wnt signalling, J. Cell. Mol. Med. 14 (2010) 1845–1856, doi:10.1111/j.1582-4934.2009.00807.x.
[46] L.F. Mendes, W.L. Tam, Y.C. Chai, L. Geris, F.P. Luyten, S.J. Roberts, Combinatorial analysis of growth factors reveals the contribution of bone morphogenetic proteins to chondrogenic differentiation of human periosteal cells, Tissue Eng. Part C Methods 22 (2016) 473–486, doi:10.1089/ten.tec.2015.0436.
[47] C.A. Schneider, W.S. Rasband, K.W. Eliceiri, NIH Image to ImageJ: 25 years of image analysis, Nat. Methods 9 (2012) 671–675, doi:10.1038/nmeth.2089.
[48] K.J. Livak, T.D. Schmittgen, Analysis of relative gene expression data using real-time quantitative PCR and, Methods 25 (2001) 402–408, doi:10.1006/meth.2001.1262.
[49] N. Van Gastel, S. Stegen, I. Stockmans, K. Moermans, J. Schrooten, D. Graf, F.P. Luyten, G. Carmeliet, Expansion of murine periosteal progenitor cells with fibroblast growth factor 2 reveals an intrinsic endochondral ossification program mediated by bone morphogenetic protein 2, Stem Cells 32 (2014) 2407–2418, doi:10.1002/stem.1783.
[50] W.L. Tam, L.Freitas Mendes, X. Chen, R. Lesage, I. Van Hoven, E. Leysen, G. Kerckhofs, K. Bosmans, Y.C. Chai, A. Yamashita, N. Tsumaki, L. Geris, S.J. Roberts, F.P. Luyten, Human pluripotent stem cell-derived cartilaginous organoids promote scaffold-free healing of critical size long bone defects, Stem Cell Res. Ther. 12 (2021) 1–16, doi:10.1186/s13287-021-02580-7.
[51] G. Fernandez de Grado, L. Keller, Y. Idoux-Gillet, Q. Wagner, A.M. Musset, N. Benkirane-Jessel, F. Bornert, D. Offner, Bone substitutes: a review of their characteristics, clinical use, and perspectives for large bone defects management, J. Tissue Eng. 9 (2018) 1–18, doi:10.1177/2041731418776819.
[52] J. Lammens, M. Maréchal, H. Delport, H. Oppermann, S. Vukicevic, F.P. Luyten, A cell-based combination product for the repair of large bone defects, Bone (2020) 115511, doi:10.1016/j.bone.2020.115511.
[53] J. Kim, E. Bakirci, K.L. O'Neill, A. Hrynevich, P.D. Dalton, Fiber bridging during melt electrowriting of poly(ε-Caprolactone) and the influence of fiber diameter and wall height, Macromol. Mater. Eng. 306 (2021), doi:10.1002/mame.202000685.
[54] F.M. Wunner, M.L. Wille, T.G. Noonan, O. Bas, P.D. Dalton, E.M. De-Juan-Pardo, D.W. Hutmacher, Melt electrospinning writing of highly ordered large volume scaffold architectures, Adv. Mater. 30 (2018), doi:10.1002/adma.201706570.
[55] R. McMaster, C. Hoefner, A. Hrynevich, C. Blum, M. Wiesner, K. Wittmann, T.R. Dargaville, P. Bauer-Kreisel, J. Groll, P.D. Dalton, T. Blunk, Tailored melt electrowritten scaffolds for the generation of sheet-like tissue constructs from multicellular spheroids, Adv. Healthc. Mater. 8 (2019), doi:10.1002/adhm.201801326.
[56] A. Hrynevich, B. Elçi, J.N. Haigh, R. McMaster, A. Youssef, C. Blum, T. Blunk, G. Hochleitner, J. Groll, P.D. Dalton, Dimension-based design of melt electrowritten scaffolds, Small 14 (2018) 1–6, doi:10.1002/smll.201800232.
[57] A. Dufour, X.B. Gallostra, C. O'Keeffe, K. Eichholz, S. Von Euw, O. Garcia, D.J. Kelly, Integrating melt electrowriting and inkjet bioprinting for engineering structurally organized articular cartilage, Biomaterials 283 (2022), doi:10.1016/j.biomaterials.2022.121405.
[58] N. Abbasi, S. Ivanovski, K. Gulati, R.M. Love, S. Hamlet, Role of offset and gradient architectures of 3-D melt electrowritten scaffold on differentiation and mineralization of osteoblasts, Biomater. Res. 24 (2020) 1–16, doi:10.1186/s40824-019-0180-z.
[59] A. Gleadall, D. Visscher, J. Yang, D. Thomas, J. Segal, Review of additive manufactured tissue engineering scaffolds: relationship between geometry and performance, Burn. Trauma 6 (2018) 1–16, doi:10.1186/s41038-018-0121-4.
[60] A. Di Luca, K. Szlazak, I. Lorenzo-Moldero, C.A. Ghebes, A. Lepedda, W. Swieszkowski, C. Van Blitterswijk, L. Moroni, Influencing chondrogenic differentiation of human mesenchymal stromal cells in scaffolds displaying a structural gradient in pore size, Acta Biomater. (2016), doi:10.1016/j.actbio.2016.03.014.
[61] A. Petersen, A. Princ, G. Korus, A. Ellinghaus, H. Leemhuis, A. Herrera, A. Klaumünzer, S. Schreivogel, A. Woloszyk, K. Schmidt-Bleek, S. Geissler, I. Heschel, G.N. Duda, A biomaterial with a channel-like pore architecture induces endochondral healing of bone defects, Nat. Commun. 9 (2018), doi:10.1038/s41467-018-06504-7.
[62] C. Colnot, Skeletal cell fate decisions within periosteum and bone marrow during bone regeneration, J. Bone Miner. Res. 24 (2009) 274–282, doi:10.1359/jbmr.081003.
[63] O. Duchamp de Lageneste, A. Julien, R. Abou-Khalil, G. Frangi, C. Carvalho, N. Cagnard, C. Cordier, S.J. Conway, C. Colnot, Periosteum contains skeletal stem cells with high bone regenerative potential controlled by Periostin, Nat. Commun. 9 (2018) 773, doi:10.1038/s41467-018-03124-z.
[64] K. Pelttari, A. Winter, E. Steck, K. Goetzke, T. Hennig, B.G. Ochs, T. Aigner, W. Richter, Premature induction of hypertrophy during *in vitro* chondrogenesis of human mesenchymal stem cells correlates with calcification and vascular invasion after ectopic transplantation in SCID mice, Arthritis Rheum 54 (2006) 3254–3266, doi:10.1002/art.22136.
[65] E. Farrell, S.K. Both, K.I. Odörfer, W. Koevoet, N. Kops, F.J. O'Brien, R.J.B. De Jong, J.A. Verhaar, V. Cuijpers, J. Jansen, R.G. Erben, G.J.V.M. Van Osch, *In-vivo* generation of bone via endochondral ossification by *in-vitro* chondrogenic priming of adult human and rat mesenchymal stem cells, BMC Musculoskelet. Disord. 12 (2011) 31, doi:10.1186/1471-2474-12-31.
[66] C. Scotti, B. Tonnarelli, A. Papadimitropoulos, A. Scherberich, S. Schaeren, A. Schauerte, J. Lopez-Rios, R. Zeller, A. Barbero, I. Martin, Recapitulation of endochondral bone formation using human adult mesenchymal stem cells as a paradigm for developmental engineering, Proc. Natl. Acad. Sci. U. S. A. 107 (2010) 7251–7256, doi:10.1073/pnas.1000302107.
[67] J. van der Stok, M.K.E. Koolen, H. Jahr, N. Kops, J.H. Waarsing, H. Weinans, O.P. van der Jagt, Chondrogenically differentiated mesenchymal stromal cell pellets stimulate endochondral bone regeneration in critical-sized bone defects, Eur. Cells Mater. 27 (2014) 137–148.
[68] C. Scotti, E. Piccinini, H. Takizawa, A. Todorov, P. Bourgine, A. Papadimitropoulos, A. Barbero, M.G. Manz, I. Martin, Engineering of a functional bone organ through endochondral ossification, Proc. Natl. Acad. Sci. U. S. A. 110 (2013) 3997–4002, doi:10.1073/pnas.1220108110.
[69] E.J. Sheehy, T. Mesallati, T. Vinardell, D.J. Kelly, Engineering cartilage or endochondral bone: a comparison of different naturally derived hydrogels, Acta Biomater. 13 (2015) 245–253, doi:10.1016/j.actbio.2014.11.031.
[70] C. Stüdle, Q. Vallmajó-Martín, A. Haumer, J. Guerrero, M. Centola, A. Mehrkens, D.J. Schaefer, M. Ehrbar, A. Barbero, I. Martin, Spatially confined induction of endochondral ossification by functionalized hydrogels for ectopic engineering of osteochondral tissues, Biomaterials 171 (2018) 219–229, doi:10.1016/j.biomaterials.2018.04.025.
[71] H.E. Weiss-Bilka, M.E. McGann, M.J. Meagher, R.K. Roeder, D.R. Wagner, Ectopic models for endochondral ossification: comparing pellet and alginate bead culture methods, J. Tissue Eng. Regen. Med. 12 (2018) e541–e549, doi:10.1002/term.2324.
[72] J. Visser, D. Gawlitta, K.E.M. Benders, S.M.H. Toma, B. Pouran, P.R. van Weeren, W.J.A. Dhert, J. Malda, Endochondral bone formation in gelatin methacrylamide hydrogel with embedded cartilage-derived matrix particles, Biomaterials 37 (2015) 174–182, doi:10.1016/j.biomaterials.2014.10.020.
[73] C.A. Knuth, J. Witte-Bouma, Y. Ridwan, E.B. Wolvius, E. Farrell, Mesenchymal stem cell-mediated endochondral ossification utilising micropellets and brief

chondrogenic priming, Eur. Cells Mater. 34 (2017) 142–161, doi:10.22203/eCM.v034a10.
[74] K. Fritsch, S. Pigeot, X. Feng, P.E. Bourgine, T. Schroeder, I. Martin, M.G. Manz, H. Takizawa, Engineered humanized bone organs maintain human hematopoiesis *in vivo*, Exp. Hematol. (2018), doi:10.1016/j.exphem.2018.01.004.
[75] R.L. Huang, J. Guerrero, A.S. Senn, E.A. Kappos, K. Liu, Q. Li, D. Dufrane, D.J. Schaefer, I. Martin, A. Scherberich, Dispersion of ceramic granules within human fractionated adipose tissue to enhance endochondral bone formation, Acta Biomater. 102 (2020) 458–467, doi:10.1016/j.actbio.2019.11.046.
[76] R. Osinga, N. Di Maggio, A. Todorov, N. Allafi, A. Barbero, F. Laurent, D.J. Schaefer, I. Martin, A. Scherberich, Generation of a bone organ by human adipose-derived stromal cells through endochondral ossification, Stem Cells Transl. Med. 5 (2016) 1090–1097, doi:10.5966/sctm.2015-0256.
[77] A. Matsiko, E.M. Thompson, C. Lloyd-Griffith, G.M. Cunniffe, T. Vinardell, J.P. Gleeson, D.J. Kelly, F.J. O'Brien, An endochondral ossification approach to early stage bone repair: Use of tissue-engineered hypertrophic cartilage constructs as primordial templates for weight-bearing bone repair, J. Tissue Eng. Regen. Med. 12 (2018) e2147–e2150, doi:10.1002/term.2638.
[78] M.B. Albro, R.J. Nims, K.M. Durney, A.D. Cigan, J.J. Shim, G. Vunjak-Novakovic, C.T. Hung, G.A. Ateshian, Heterogeneous engineered cartilage growth results from gradients of media-supplemented active TGF-β and is ameliorated by the alternative supplementation of latent TGF-β, Biomaterials 77 (2016) 173–185, doi:10.1016/j.biomaterials.2015.10.018.
[79] M. Sarem, O. Otto, S. Tanaka, V.P. Shastri, Cell number in mesenchymal stem cell aggregates dictates cell stiffness and chondrogenesis, (2019) 1–18.
[80] N.T. Saidy, F. Wolf, O. Bas, H. Keijdener, D.W. Hutmacher, P. Mela, E.M. De-Juan-Pardo, Biologically inspired scaffolds for heart valve tissue engineering via melt electrowriting, Small 15 (2019) 1–15, doi:10.1002/smll.201900873.
[81] O. Guillaume, O. Kopinski-Grünwald, G. Weisgrab, T. Baumgartner, A. Arslan, K. Whitmore, S. Van Vlierberghe, A. Ovsianikov, Hybrid spheroid microscaffolds as modular tissue units to build macro-tissue assemblies for tissue engineering, Acta Biomater. (2022), doi:10.1016/j.actbio.2022.03.010.
[82] K.R. Silva, R.A. Rezende, F.D.A.S. Pereira, P. Gruber, M.P. Stuart, A. Ovsianikov, K. Brakke, V. Kasyanov, V. Jorge, M. Granjeiro, L.S. Baptista, V. Mironov, L. Silva, Delivery of human adipose stem cells spheroids into lockyballs, PLoS One 11 (2016) 1–14, doi:10.1371/journal.pone.0166073.
[83] R. Sinha, M. Cámara-Torres, P. Scopece, E. Verga Falzacappa, A. Patelli, L. Moroni, C. Mota, A hybrid additive manufacturing platform to create bulk and surface composition gradients on scaffolds for tissue regeneration, Nat. Commun. 12 (2021), doi:10.1038/s41467-020-20865-y.
[84] J.E. Bergsma, W.C. de Bruijn, F.R. Rozema, R.R.M. Bos, G. Boering, Late degradation tissue response to poly(l-lactide) bone plates and screws, Biomaterials 16 (1995), doi:10.1016/0142-9612(95)91092-D.
[85] H. Winet, J.O. Hollinger, Incorporation of polylactide–polyglycolide in a cortical defect: neoosteogenesis in a bone chamber, J. Biomed. Mater. Res. 27 (1993), doi:10.1002/jbm.820270514.
[86] M. Bartnikowski, T.R. Dargaville, S. Ivanovski, D.W. Hutmacher, Degradation mechanisms of polycaprolactone in the context of chemistry, geometry and environment, Prog. Polym. Sci. 96 (2019), doi:10.1016/j.progpolymsci.2019.05.004.
[87] B.K. Hall, Divide, accumulate, differentiate : cell condensation In skeletal development, Int. J. Dev. Biol. 39 (1995) 881–893 http://www.ijdb.ehu.es/web/paper.php?doi=8901191.
[88] C. Maes, G. Carmeliet, E. Schipani, Hypoxia-driven pathways in bone development, regeneration and disease, Nat. Rev. Rheumatol. 8 (2012) 358–366, doi:10.1038/nrrheum.2012.36.
[89] H. Kronenberg, Developmental regulation of the growth plate, Nature 423 (2003) 332–336.
[90] H.E. Owston, K.M. Moisley, G. Tronci, S.J. Russell, P.V. Giannoudis, E. Jones, Induced periosteum-mimicking membrane with cell barrier and multipotential stromal cell (MSC) homing functionalities, Int. J. Mol. Sci. 21 (2020) 1–16, doi:10.3390/ijms21155233.